Progress In Electromagnetics Research B, Vol. 118, 87–103, 2026

(Received 11 May 2026, Accepted 20 June 2026, Scheduled 8 August 2026)

Multi-Objective Optimization of Rare-Earth-Saving Permanent Magnet Generator with Asymmetric Poles Based on Sensitivity Analysis

Yanhong Gao[1], Huihui Geng[2,*], Xingzhe Pang[3], Wenyu Li[2], Junfeng Wang[4], Xin Zhou[2], and Xingxu Jin[2]

[1]*Shandong Tangjun Ouling Automobile Manufacturing Co., Ltd., Zibo 255000, China*
[2]*School of Transportation and Vehicle Engineering, Shandong University of Technology, Zibo 255049, China*
[3]*Weichai Power Co., Ltd., Weifang 261061, China*
[4]*Shandong Shouda Automobile Manufacturing Co., Ltd., Linyi 276200, China*

ABSTRACT: To cut rare-earth consumption and suppress cogging torque of conventional symmetrical pole permanent magnet generator (PMG) systems, this paper presents a low-rare-earth composite asymmetric pole topology with hybrid NdFeB-ferrite magnets. The magnetic-field modulation of permanent magnet magnetomotive force (MMF) is analyzed, and an energy-method cogging torque formula is derived to elaborate the flux-improving and torque-reducing mechanism of asymmetric poles. Equivalent magnetic circuit and finite element models are built, followed by stratified sensitivity analysis of structural parameters. Taking high induced electromotive force (EMF), low EMF THD, and small cogging torque as targets, magnet arc angle is optimized via an evolutionary algorithm coupled with TOPSIS; magnet width and thickness are further optimized for optimal cost-performance. After optimization, EMF fundamental amplitude rises; EMF THD and cogging torque drop; and NdFeB usage falls by 8.56%. Prototype tests verify the simulation accuracy. The hybrid magnet scheme saves rare-earth materials and enhances overall generator performance.

1. INTRODUCTION

Automotive generators supply electrical power to the vehicle's lighting, steering, starting, electrical, and electronic control systems, serving as the sole source of power for all the vehicle's electrical equipment.

In the current era, characterized by trends towards intelligence, connectivity, and electrification, the variety and power consumption of automotive electrical devices continue to increase [1]. With the increasing production of new energy vehicles, the annual application volume of rare-earth permanent magnet (PM) NdFeB has also increased. However, NdFeB prices have fluctuated significantly. In contrast, non-rare-earth PM ferrites offer lower costs and a more stable market supply, albeit with a lower remanent flux density [2, 3]. The construction of hybrid poles by combining NdFeB and ferrite excitation forms a rare-earth-saving pole structure. This approach can reduce NdFeB consumption while maintaining generator performance. Rare-earth-saving permanent magnet generators (PMGs) feature high efficiency, high reliability, and low manufacturing cost, representing an important development direction for PMGs [4, 5].

Currently, numerous scholars have researched PMGs and their electromagnetic characteristics, achieving significant results. Ref. [6] indicates that under identical generator volume constraints, a built-in double-V pole structure achieves flux concentration through pole combination, thereby increasing air-gap flux density amplitude. It also enhances the magnetomotive force (MMF) of the magnetic circuit via MMF series connection, consequently improving power density. However, this structure increases both rare-earth material usage and cogging torque. Ref. [7] proposes an alternating-pole PMG, reducing NdFeB consumption. Nevertheless, the air-gap flux density waveform of this generator exhibits significant asymmetry, low amplitude, high waveform distortion, and poor output performance. Ref. [8] introduces a novel PMG employing magnetic shunting poles on both sides of the PMs to alter leakage flux paths and improve the sinusoidal quality of the induced electromotive force (EMF) waveform. However, the addition of these poles increases leakage flux and reduces PM utilization. Ref. [9] presents a rare-earth-saving stator-PM flux-switching generator. This design employs partial non-rare-earth ferrite PMs on the stator, supplemented by an appropriate amount of rare-earth NdFeB PMs, reducing rare-earth material usage and manufacturing costs while meeting output performance targets. However, the PMs embedded within the stator and located amidst the armature windings can easily cause saturation in the stator core magnetic circuit. To compensate for ferrite's low energy product and remanent flux density, Ref. [10] proposes a Halbach-array rare-earth-saving PMG. By modifying the PM arrangement, tangential and radial PMs are closely connected to form a Halbach array to enhance the effective air-gap flux. However, the Halbach array presents high manufacturing difficulty, stringent requirements for radial and tangential PM arrangements, increased manufacturing costs, and certain limitations in engineering applications.

* Corresponding author: Huihui Geng (huihuigeng@sdut.edu.cn).

doi:10.2528/PIERB26051102

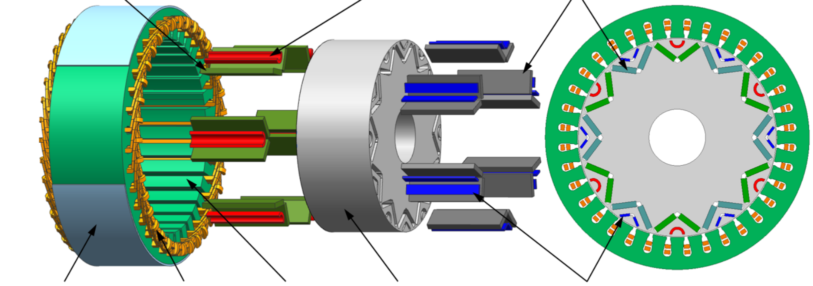

FIGURE 1. Rare-earth-saving hybrid pole structure.

Based on the above analysis and considering specific engineering applications, this study takes automotive PMG as the research object. Building upon the double-V hybrid pole structure, per pole pair, the first rectangular PM uses ferrite, and the other three PMs employ NdFeB. This configuration constitutes the proposed rare-earth-saving hybrid pole structure with combined NdFeB and ferrite excitations. The parameters of the rare-earth-saving PMG are listed in Table 1, and its hybrid pole structure is illustrated in Figure 1.

2. ANALYSIS OF AIR GAP FIELD MODULATION MECHANISM IN ASYMMETRIC POLES

2.1. Analytical Modeling of Air Gap Flux Density Based on MMF

Neglecting the modulation effect of stator slots on the air-gap magnetic field, the MMF produced by a single PM is a square-wave function of the mechanical angle [11]. Within the double-V hybrid pole structure, the PMs in a single pole can be categorized into two pairs of rectangular PMs: one pair positioned at the outer periphery of the pole forms a large V-shaped PM set, whereas the other pair located towards the inner part of the pole forms a small V-shaped PM set.

The resultant MMF of the hybrid pole structure, as a function of the generator's mechanical angle θ_g function $F_{mp}(\theta_g)$, can be expressed as:

$$F_{mp}(\theta_g) = \begin{cases} 0, & (m-1)\dfrac{360^\circ}{2p} \le \theta_g \le m\dfrac{(1-\alpha_p)\,360^\circ}{4p} \\ (-1)^{m-1} F_{m1}, & m\dfrac{(1-\alpha_p)\,360^\circ}{4p} \le \theta_g \le m\dfrac{(1-\alpha_v)\,360^\circ}{4p} \\ (-1)^{m-1}(F_{m1}+F_{m2}), & m\dfrac{(1-\alpha_v)\,360^\circ}{4p} \le \theta_g \le m\dfrac{(1+\alpha_v)\,360^\circ}{4p} \\ (-1)^{m-1} F_{m1}, & m\dfrac{(1+\alpha_v)\,360^\circ}{4p} \le \theta_g \le m\dfrac{(1+\alpha_p)\,360^\circ}{4p} \\ 0, & m\dfrac{(1+\alpha_p)\,360^\circ}{4p} \le \theta_g \le m\dfrac{360^\circ}{2p} \end{cases} \quad \{m|1 \le m \le 2p, m \in N+\} \tag{1}$$

where F_{m1} is the MMF of the first rectangular PM; F_{m2} is the MMF of the series connection of the first and second rectangular PMs; α_p is the pole arc coefficient of the rotor pole, representing the angle corresponding to the first rectangular PMs; α_v is the pole arc coefficient corresponding to the small V-shaped PM set, which represents the central angle of the second rectangular PMs; and p is the number of pole pairs of the generator. The mechanical angle of the generator θ_g is shown in Figure 2.

Based on Ohm's law for magnetic circuits and the definitional formula of magnetic flux:

$$B_{mp}(\theta_g) = \frac{F_{mp}(\theta_g)\,G}{A_f} \tag{2}$$

where $B_{mp}(\theta_g)$ is the combined pole magnetic induction as a function of the mechanical angle; G is the equivalent permeance of the magnetic circuit; and A_f is the effective area through which the magnetic flux passes.

From Equations (1) and (2), $B_{mp}(\theta_g)$ is a periodic function with a period equal to $360^\circ/2p$, which indicates that the permanent magnet MMF has a direct influence on the air-gap magnetization. By improving the distribution of the magnetic potential of the excitation source, the distribution function of the magnetic induction intensity of the combined poles can be improved, which in turn improves the air-gap magnetization distribution.

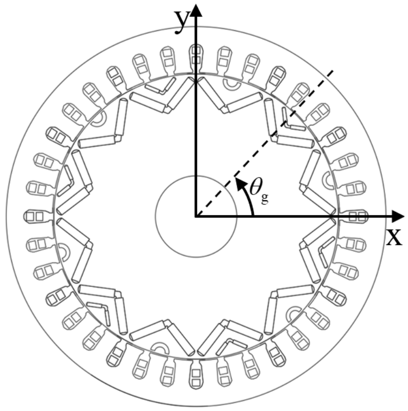

FIGURE 2. Generator's mechanical angle.

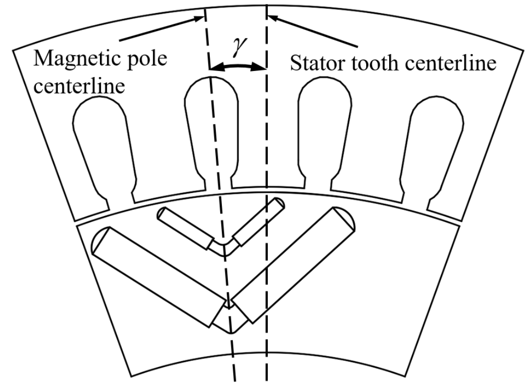

FIGURE 3. Relative position of the stator and rotor.

2.2. Weakening Mechanism of Cogging Torque Based on Improving the Air-Gap Magnetic Field

The cogging torque of a PMG is the torque produced by the magnetic field generated by PMs acting with the stator cogging when the armature winding is open-circuited [12]. A large cogging torque can cause the generator's rotating shaft, bearings, and other mechanical components to withstand cyclical changes in force, increasing mechanical wear and shortening generator life. Automotive PMGs should attempt to reduce cogging torque.

The cogging torque T_{cog} is the negative derivative of the generator magnetic-field energy W at no load to the relative stator-rotor position angle γ [13]:

$$T_{cog}(\gamma) = -\frac{\partial W(\gamma)}{\partial \gamma} \tag{3}$$

The stator and rotor cores are made of silicon steel, whose relative permeability is approximately 7000~9000. Assuming that the permeability of the core is infinite, the generator magnetic field energy can be approximated as [14]:

$$W \approx W_{air} = \frac{1}{2\mu_0}\int_V B_r^2(\theta_g,\gamma)dV \tag{4}$$

where W_{air} is the air-gap magnetic field energy; μ_0 is the vacuum permeability with a magnitude of $4\pi \times 10^{-7}$ H/m; $B_r(\theta_g,\gamma)$ is the distribution function of the air-gap magnetic density along the air-gap circumference; and V is the generator main air-gap volume. The relative position angle, γ, between the generator's stator and rotor are shown in Figure 3.

In Equation (4), $B_r(\theta_g,\gamma)$ can be expressed as:

$$\begin{aligned} B_r(\theta_g,\gamma) &= B_{mp}(\theta_g)\, G_\delta(\theta_g,\gamma) \\ &= B_{mp}(\theta_g)\frac{h_m(\theta_g)}{h_m(\theta_g)+\delta(\theta_g,\gamma)} \end{aligned} \tag{5}$$

where $G_\delta(\theta_g,\gamma)$ is the distribution function of the relative air-gap permeance along the air-gap circumference; $h_m(\theta_g)$ is the height of the magnetization direction of the PM as a function of the mechanical angle; and $\delta(\theta_g,\gamma)$ is the distribution function of the main air-gap length along the air-gap circumference.

TABLE 1. Parameters of the rare-earth-saving PMG.

Parameter	Value
Rated power/kW	1
Rated voltage/V	28
Rated speed/r/min	4000
Number of phases	3
Number of pole pairs	6
Number of stator slots	36
Axial length of the PMG/mm	40
Outer diameter of the stator/mm	140
Inner diameter of the stator/mm	106
Length of the main air gap/mm	0.5

Substituting Equation (5) into Equation (4) yields:

$$W_{air} = \frac{1}{2\mu_0}\int_0^{l_{ef}}\int_{r_{s1}}^{r_{s2}}\int_0^{2\pi} B_{mp}^2(\theta_g)\left[\frac{h_m(\theta_g)}{h_m(\theta_g)+\delta(\theta_g,\gamma)}\right]^2 d\theta_g r dr dl \tag{6}$$

where l_{ef} is the axial length of the core; r_{s2} is the outer radius of the rotor; and r_{s1} is the inner radius of the stator.

Fourier decomposition of $B_{mp}^2(\theta_g)$ and $\left[\frac{h_m(\theta_g)}{h_m(\theta_g)+\delta(\theta_g,\gamma)}\right]^2$ respectively gives:

$$\begin{cases} B_{mp}^2(\theta_g) = B_{mp0} + \sum\limits_{n=1}^{\infty} B_{mpn}\cos 2np\theta_g \\ \left[\frac{h_m(\theta_g)}{h_m(\theta_g)+\delta(\theta_g,\gamma)}\right]^2 = G_{\delta 0} + \sum\limits_{n=1}^{\infty} G_{\delta n}\cos nZ(\theta_g+\gamma) \end{cases} \tag{7}$$

where B_{mp0} is the constant term of the Fourier decomposition of the squared function of the magnetic induction intensity; B_{mpn} is the nth Fourier expansion coefficient of the squared function of the magnetic induction intensity; $G_{\delta 0}$ is the constant term of the Fourier decomposition of the squared function of the relative air gap permeance; and $G_{\delta n}$ is the nth Fourier expansion coefficient of the squared function of the relative air gap permeance.

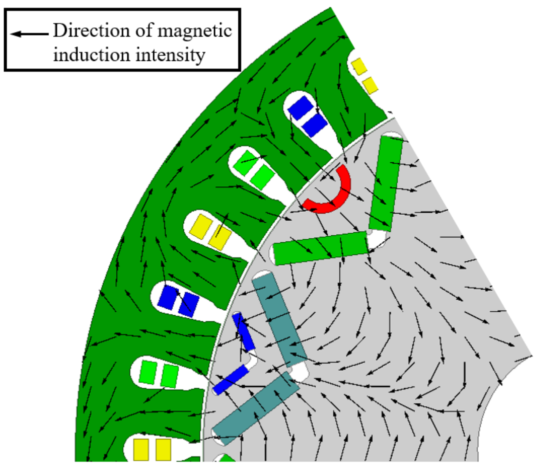

FIGURE 4. Magnetic flux density orientation of the rare-earth-saving PMG.

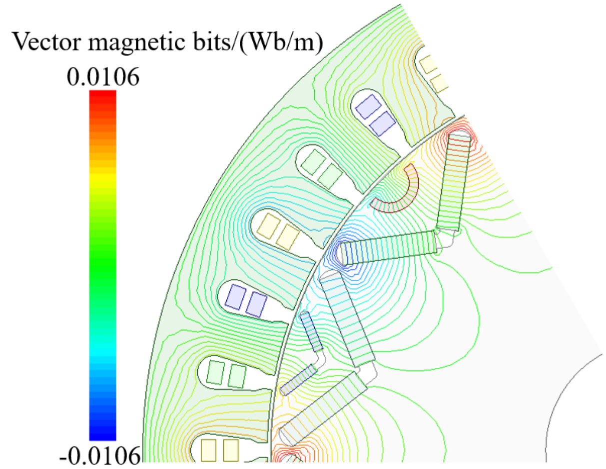

FIGURE 5. Flux line distribution of the rare-earth-saving PMG.

In Equation (7) [15]:

$$\begin{cases} B_{mp0} = \alpha_p B_{mp}^2 \\ B_{mpn} = \frac{2}{n\pi} B_{mp}^2 \sin(n\alpha_p \pi) \end{cases} \tag{8}$$

where B_{mp} is the combined pole magnetic induction.

Substituting Equations (7) and (8) into Equation (6), and then substituting Equations (4), (5), and (6) into Equation (3), the expression for the cogging torque can be obtained as follows:

$$T_{cog}(\gamma) = \frac{\pi Z l_{ef}}{4\mu_0} \left(r_{s2}^2 - r_{s1}^2\right) \sum_{n=1}^{\infty} n G_{\delta n} B_{mp(nZ/2p)} \sin(nZ\gamma) \tag{9}$$

From Equation (9), under the premise of not changing the design dimensions of the generator core length, number of stator slots, and other technical indicators, the method of weakening the cogging torque is mainly through the improvement of the magnetic induction intensity of magnetic poles as a function of the distribution in the circumference. The permanent magnet MMF directly influences the magnetic induction intensity of the poles. Therefore, by improving the MMF of PMs, it is possible to reduce the cogging torque in PMGs while optimizing the air-gap flux density distribution and maintaining the generator's output performance.

3. ELECTROMAGNETIC CHARACTERISTICS ANALYSIS OF RARE-EARTH-SAVING PMG

3.1. Magnetic Circuit Distribution Analysis and Equivalent Magnetic Circuit Modeling

Based on the preliminary topology of the rare-earth-saving PMG, the magnetic flux density orientation and flux line distribution were obtained through static magnetic-field simulation, as shown in Figures 4 and 5, respectively.

According to the relationship between the direction of the magnetic induction intensity in Figure 4 and series and parallel connections of the excitation source in Figure 5, the magnetic circuit through the main air gap in the rare-earth-saving PMG can be split into two parts: the main magnetic circuit consisting of the N-pole first rectangular ferrite PM and the S-pole third rectangular NdFeB PM connected in series, and the second consisting of all the PMs under one pair of poles connected in series. A schematic of the magnetic circuit of the rare-earth-saving PMG is shown in Figure 6.

The PMs generate magnetic flux, and permeance exists in each PM, the iron core, and the air gap. With the initial position of the magnetic circuit of the first rectangular ferrite PM N-pole, the magnetic circuit distribution of the rare-earth-saving PMG is:

Main magnetic circuit 1: Starting from the first rectangular ferrite PM N-pole, the magnetic flux passes through rotor core, main air gap, stator teeth, stator yoke, stator teeth, main air gap, rotor core, third rectangular NdFeB PM, rotor core, and finally returns to the first rectangular ferrite PM S-pole.

Main magnetic circuit 2: Starting from the first rectangular ferrite PM N-pole, the magnetic flux passes through rotor core, second rectangular NdFeB PM, rotor core, main air gap, stator teeth, stator yoke, stator teeth, main air gap, rotor core, arc-shaped NdFeB PM, rotor core, third rectangular NdFeB PM, rotor core, and finally returns to the S-pole of the first rectangular ferrite PM.

Each leakage circuit: from each PM N-pole, through the rotor core, to each PM S-pole.

Based on the analysis of the magnetic circuit and using the principle of superposition of magnetic circuits, the equivalent magnetic circuit model of the rare-earth-saving PMG was obtained, as shown in Figure 7.

The definitions of each MMF, flux, and permeance in Figure 7 are as follows:

F_{st} is the direct-axis armature reaction MMF, F_{st} =0 under no-load condition. F_1, F_2, F_3, F_4 are the MMF of the first rectangular PM, the second rectangular PM, the third rectangular PM, and the arc-shaped PM, respectively.

Φ_1, Φ_2 are the magnetic fluxes of main magnetic circuit 1 and main magnetic circuit 2, respectively. Φ_{lea1}, Φ_{lea2}, Φ_{lea3},

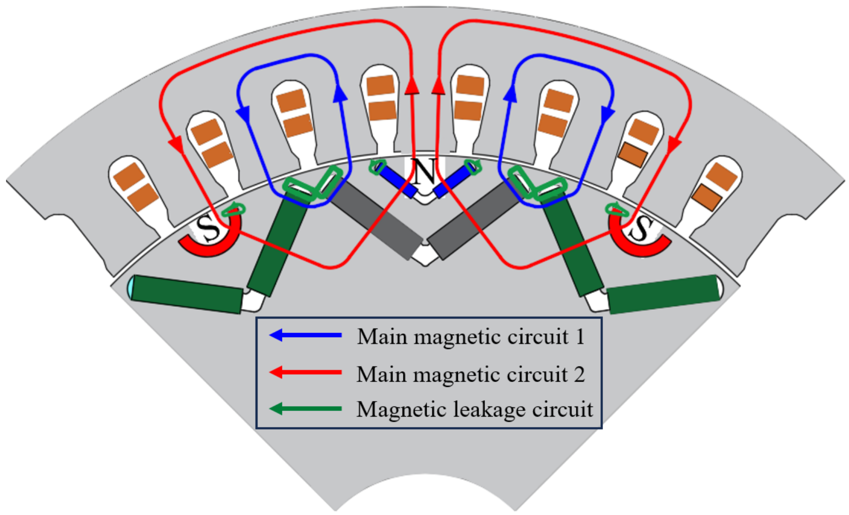

FIGURE 6. Magnetic circuit of the rare-earth-saving PMG.

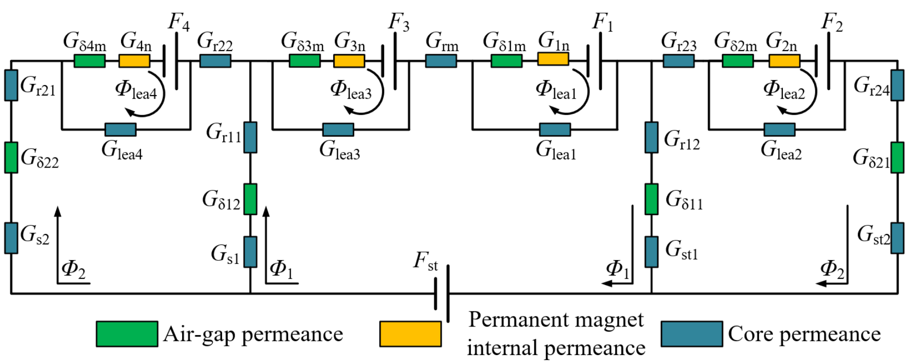

FIGURE 7. Equivalent magnetic circuit model of the rare-earth-saving PMG.

Φ_{lea4} are the leakage fluxes of the first rectangular PM, the second rectangular PM, the third rectangular PM, and the arc-shaped PM, respectively.

$G_{1n}, G_{2n}, G_{3n}, G_{4n}$ are the internal permeances of the first rectangular PM, the second rectangular PM, the third rectangular PM, and the arc-shaped PM, respectively. G_{r11} and G_{r12} are the permeances between the air gap and the third rectangular PM, and between the first rectangular PM and the air gap in main magnetic circuit 1, respectively. $G_{r21}, G_{r22}, G_{rm}, G_{r23}$, and G_{r24} are the permeances between the air gap and the arc-shaped PM, between the arc-shaped PM and the third rectangular PM, between the third rectangular PM and the first rectangular PM, between the first rectangular PM and the second rectangular PM, and between the second rectangular PM and the air gap in the main magnetic circuit 2, respectively. G_{lea1}, $G_{lea2}, G_{lea3}, G_{lea4}$ are the permeances of the leakage circuit of the first rectangular PM, the second rectangular PM, the third rectangular PM, and the arc-shaped PM, respectively. $G_{\delta 11}$, $G_{\delta 12}$ are the air gap permeances between the N-pole and the stator teeth, and between the stator teeth and the S-pole in main magnetic circuit 1, respectively. $G_{\delta 21}$ and $G_{\delta 22}$ are the air-gap permeances between the N-pole and the stator teeth, and between the stator teeth and the S-pole in the main magnetic circuit 2, respectively. G_{s1} and G_{s2} are the stator yoke permeances in main magnetic circuit 1 and main magnetic circuit 2, respectively. G_{st1} and G_{st2} are the stator tooth permeances in the main magnetic circuit 1 and main magnetic circuit 2, respectively. $G_{\delta 1m}, G_{\delta 2m}, G_{\delta 3m}, G_{\delta 4m}$ are the permeances of the assembly gaps between the first rectangular PM and the rotor core, between the second rectangular PM and the rotor core, between the third rectangular PM and the rotor core, and between the arc-shaped PM and the rotor core, respectively.

Based on Ohm's law and Kirchhoff's law for magnetic circuits, a system of flux equations for magnetic circuits is presented [16]:

(1) Flux equations for the main magnetic circuits

$$\left\{\begin{array}{l} F_4+\Phi_1\left(\frac{1}{G_{r11}}+\frac{1}{G_{\delta 12}}+\frac{1}{G_{s1}}\right) \\ =\Phi_2\left(\frac{1}{G_{s2}}+\frac{1}{G_{\delta 22}}+\frac{1}{G_{r21}}+\frac{1}{G_{r22}}\right) \\ +\left(\Phi_2+\Phi_{lea4}\right)\left(\frac{1}{G_{\delta 4m}}+\frac{1}{G_{4n}}\right) \\ F_1+F_3=\Phi_1\left(\frac{1}{G_{r12}}+\frac{1}{G_{\delta 11}}+\frac{1}{G_{st1}}+\frac{1}{G_{s1}}+\frac{1}{G_{\delta 12}}+\frac{1}{G_{r11}}\right) \\ +\left(\Phi_1+\Phi_2\right)\frac{1}{G_{rm}}+\left(\Phi_1+\Phi_2+\Phi_{lea1}\right)\left(\frac{1}{G_{1n}}+\frac{1}{G_{\delta 1m}}\right) \\ +\left(\Phi_1+\Phi_2+\Phi_{lea3}\right)\left(\frac{1}{G_{3n}}+\frac{1}{G_{\delta 3m}}\right)+F_{st} \\ F_2+\Phi_1\left(\frac{1}{G_{r12}}+\frac{1}{G_{\delta 11}}+\frac{1}{G_{st1}}\right)= \\ \Phi_2\left(\frac{1}{G_{st2}}+\frac{1}{G_{\delta 21}}+\frac{1}{G_{r23}}+\frac{1}{G_{r24}}+\frac{1}{G_{\delta 2m}}+\frac{1}{G_{2n}}\right) \end{array}\right. \tag{10}$$

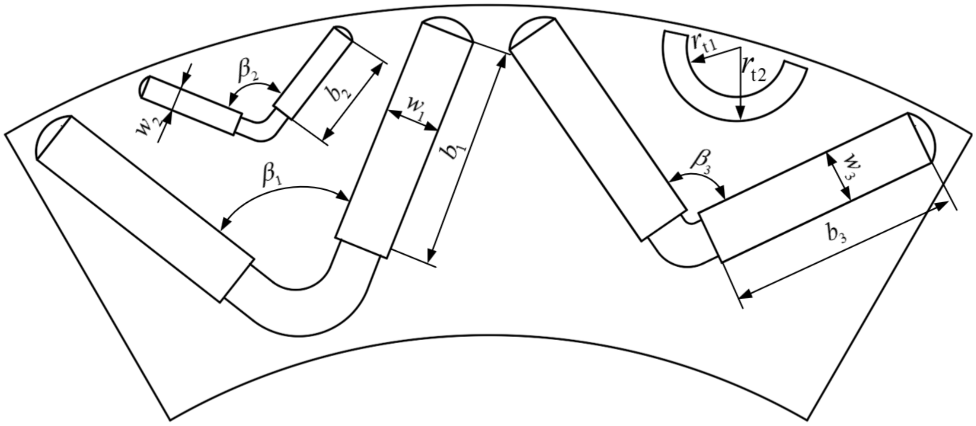

FIGURE 8. Optimization parameters.

(2) Flux equations for leakage magnetic circuits

$$\begin{cases} F_1 = \Phi_{lea1}\left(\frac{1}{G_{lea1}} + \frac{1}{G_{1n}} + \frac{1}{G_{\delta 1m}}\right) \\ F_2 = \Phi_{lea2}\left(\frac{1}{G_{lea2}} + \frac{1}{G_{2n}} + \frac{1}{G_{\delta 2m}}\right) \\ F_3 = \Phi_{lea3}\left(\frac{1}{G_{lea3}} + \frac{1}{G_{3n}} + \frac{1}{G_{\delta 3m}}\right) \\ F_4 = \Phi_{lea4}\left(\frac{1}{G_{lea4}} + \frac{1}{G_{4n}} + \frac{1}{G_{\delta 4m}}\right) \end{cases} \tag{11}$$

3.2. Determination of Optimization Parameters Based on Equivalent MMF and Permeance Pairs

In the equivalent magnetic circuit model, the equivalent MMF F can be expressed as:

$$\begin{cases} F = H_c w_{pm} \\ H_c = \left[1 + (s-20)\frac{K_{Hc}}{100}\right]\left(1 - \frac{I}{100}\right) H_{c20} \end{cases} \tag{12}$$

where H_c is the calculated coercivity of the PM; w_{pm} is the thickness of the PM magnetizing direction; s is the generator operating temperature; K_{Hc} is the reversible temperature coefficient of coercivity, $-0.18\%/^\circ$C for ferrite Y30 and $-0.5\%/^\circ$C for NdFeB N35H; I is the irreversible loss rate of coercivity, which is taken as 0% in the no-load analysis; H_{c20} is the coercivity of the PM at 20°C, which is 300 kA/m for ferrite Y30 and 1350 kA/m for NdFeB N35H.

Each equivalent permeance in the equivalent magnetic circuit model can be expressed as:

$$G = \frac{\mu_r \mu_0 A_G}{l_G} \tag{13}$$

where μ_r is the relative permeability of the material; l_G is the length of the magnetic circuit through the region of equivalent permeance; A_G is the cross-sectional area of the equivalent permeance path.

From Equations (12) and (13), the thickness and width of the PM directly affect the MMF and permeance, respectively. Meanwhile, the included angle of the V-type PM directly affects the magnitude of the core permeance in the magnetic circuit and the direction of the PM's magnetic induction intensity relative to the rotor core [17]. From this, each optimization parameter of the rare-earth-saving PMG can be selected, and a schematic diagram of the optimization parameters is shown in Figure 8. The definitions of the optimization parameters and their value ranges are listed in Table 2.

TABLE 2. Optimized range of values.

Parameter	Definition	Range
$\beta_1/^\circ$	Included angle between the first rectangular PMs	(30, 90]
$\beta_2/^\circ$	Included angle between the second rectangular PMs	[30, 100]
$\beta_3/^\circ$	Included angle between the third rectangular PMs	(30, 90]
r_{t1}/mm	Inner radius of arc-shaped PM	[2, 3)
r_{t2}/mm	Outer radius of arc-shaped PM	[3, 5]
w_1/mm	Thickness of the first rectangular PM	Based on β_1
w_2/mm	Thickness of the second rectangular PM	Based on β_2
w_3/mm	Thickness of the third rectangular PM	Based on β_3
b_1/mm	Width of the first rectangular PM	Based on β_1
b_2/mm	Width of the second rectangular PM	Based on β_2
b_3/mm	Width of the third rectangular PM	Based on β_3

The PM arrangement involves two-dimensional parameters: length and angle. To avoid the problem of dimensional interference during the optimization process, the PM angle parameters β_1, β_2, and β_3 should be determined first, and the optimized range of values for the length parameters should be determined based on the angle parameters.

4. SENSITIVITY HIERARCHICAL OPTIMIZATION OF STRUCTURAL PARAMETERS OF RARE-EARTH-SAVING PMG

4.1. Sensitivity Analysis and Determination of Hierarchical Optimization Scheme

The sensitivity of the optimization parameters to optimization objectives reflects the degree of influence of parameter changes on optimization objectives. To intuitively reflect the degree of influence of various optimization parameters on the optimization objectives, a sensitivity index was introduced. The sensitivity index of a single optimization objective can be expressed as follows:

$$S(x_i) = \left| avg \left(\frac{dg(x_i)}{dx_i} \frac{x_i}{g(x_i)} \right) \right| \tag{14}$$

where x_i is the independent variable of the optimization objective function; $g(x_i)$ is the function of the optimization objective with respect to the optimization parameters; and avg denotes the average value.

The larger the sensitivity index of an optimization parameter to the objective, the greater the parameter's influence on the objective. When optimizing this parameter, special attention should be paid to its impact on the optimization objectives. The fundamental amplitude of induced EMF E_1, the total harmonic distortion of the induced EMF waveform THD_E, and the maximum cogging torque T_{cogmax} are selected as the optimization objectives of low-rare-earth PMGs. The sensitivity analysis index of the optimization parameters to the optimization objectives can be obtained from Equation (14), and a sensitivity diagram can be drawn. The sensitivity radar chart of the rotor magnetic pole optimization parameters is shown in Figure 9.

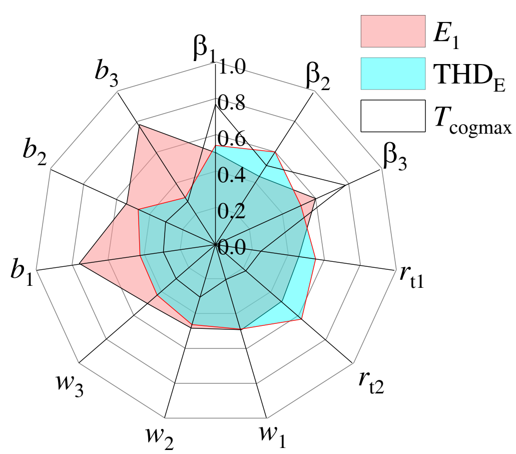

FIGURE 9. Sensitivity radar chart for rotor pole optimization parameters.

From Figure 9, for the fundamental amplitude and total harmonic distortion (THD) of the induced EMF, the sensitivity index of each optimization parameter ranges from 0.31 to 0.78, which is at a high level. For the maximum cogging torque, the sensitivity index for angles β_1, β_2 and β_3 among the three pairs of rectangular PMs ranged from 0.52 to 0.79, which is a relatively high value. The sensitivity index for the maximum cogging torque for the parameters other than β_1, β_2 and β_3 is in the range of 0.2 to 0.3, which is at a lower level. Based on this, a concise and efficient multi-objective hierarchical optimization scheme was developed. To avoid mutual interference between the PMs, the first layer of the optimization parameters for the three pairs of rectangular PM angles was selected.

In addition to the induced EMF, three pairs of rectangular PM angles on the maximum value of the cogging torque of the sensitivity analysis of the index are larger; therefore, they are selected as optimization objectives for the composition of the first layer of the optimization scheme for E_1, THD_E, and T_{cogmax}. The second layer of optimization parameters for each PM width and thickness, the PM width and thickness has a greater impact on E_1 and THD_E, has a smaller impact on T_{cogmax}, and directly affects the cost of PMs M. To simplify the optimization process, the optimization objectives of the second layer were selected for E_1 and THD_E and combined with the cost M.

4.2. Optimization of Angular Parameters Based on Evolutionary Algorithm and TOPSIS Method

The evolutionary algorithm is a type of multi-objective optimization algorithm based on the law of nature's superiority and inferiority, and its combination with the Pareto frontier optimal solution set can make the optimization objective converge to optimal conditions continuously [18]. The algorithm has the advantages of strong adaptability and high accuracy of optimization parameter screening, which is suitable for application in cases of strong coupling relationships and fewer optimization parameters.

An evolutionary algorithm is chosen to perform multi-objective optimization of the asymmetric pole parameters in the first layer of optimization variables in the following steps:

(1) Generate the initialized population, and the population individuals for the n-dimensional optimization parameters can be represented as:

$$e = [x_1, x_2, \ldots, x_n] \tag{15}$$

where x_n is each optimization parameter, and the value is randomly generated within a preset optimization range.

(2) The fitness assessment of the optimization objectives is used to select the weights of each optimization objective ξ. The weights of each optimization objective are $\xi(E_1) = 0.4$, $\xi(THD_E) = 0.3$, and $\xi(T_{cogmax}) = 0.3$ respectively, and the combined fitness function can be obtained as:

$$\begin{aligned} g(e) &= \xi(E_1) E_1(\beta_1, \beta_3) + \xi(THD_E) THD_E(\beta_1, \beta_3) \\ &\quad + \xi(T_{cogmax}) T_{cogmax}(\beta_1, \beta_3) \end{aligned} \tag{16}$$

where $E_1(\beta_1, \beta_3)$, $THD_E(\beta_1, \beta_3)$ and $T_{cogmax}(\beta_1, \beta_3)$ are the optimization objectives corresponding to the optimization parameters.

(3) Roulette wheel selection. The probability of selecting an individual can be obtained based on the composite fitness function of the individual. The larger the composite fitness function is, the more the individual meets the optimization expectations. The probability of selecting the jth individual can be expressed as:

$$Pr_j = \frac{g(e_j)}{\sum_{k=1}^{n} g(e_k)} \tag{17}$$

where e_j is the jth population individual.

(4) Set the crossover probability and perform the crossover operation to obtain the offspring population. The selected parent individuals $e(\beta'1, \beta''3)$ and $e(\beta''_1, \beta''_3)$ perform the crossover operation, and the offspring of the two are $e(\beta'_1, \beta''_3)$ and $e(\beta''_1, \beta'_3)$. In this study, the crossover

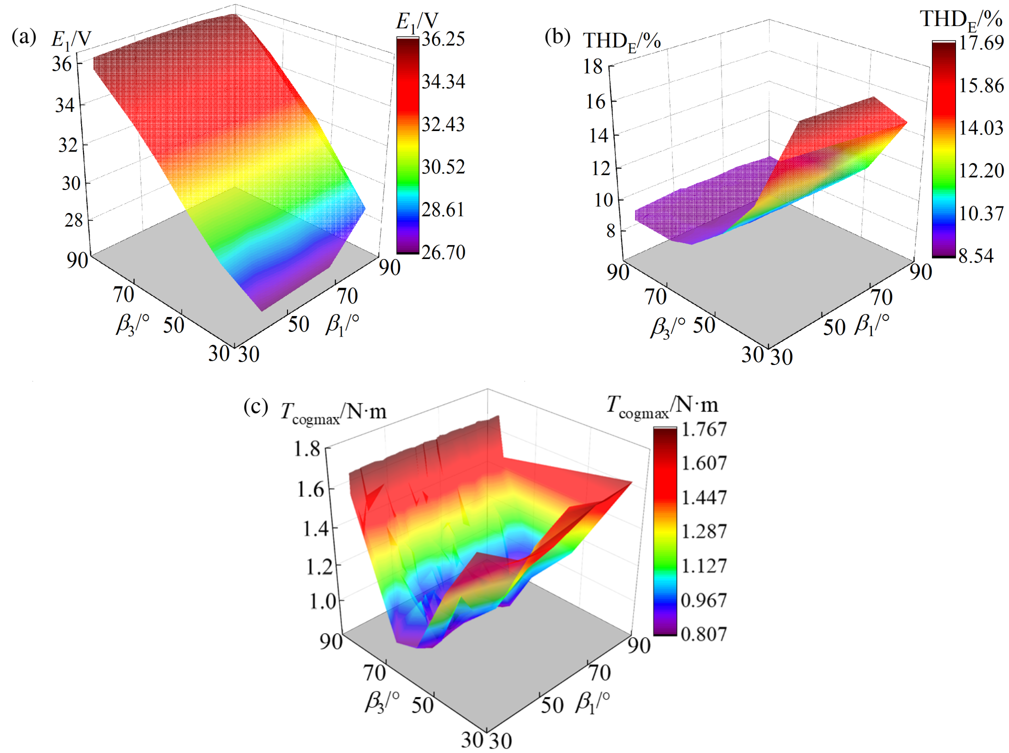

FIGURE 10. Law of influence of parameters β_1 and β_3 on E_1, THD_E and T_{cogmax}. (a) E_1, (b) THD_E, and (c) T_{cogmax}.

probability $\Pr_c$ was set to 0.8, indicating that there was an 80% chance that the selected parent individuals would undergo crossover operation.

(5) Sub-generation mutation operation. The probability of mutation in this study is taken as 1%. Corresponding to offspring individuals, to avoid the parameter value of the local optimal solution being too concentrated, the offspring population should be mutated. For example, in individual $e\left(\beta''_1, \beta''3\right)$, $\beta''1$ can be expressed as after mutation:

$$\beta'''1 = \beta''1 + (\beta_{1\,\max} - \beta_{1\,\min}) \times rand(n) \times k_j \tag{18}$$

where $\beta_{1\,\max}$ and $\beta_{1\,\min}$ are divided into the maximum and minimum values in the optimization range of β_1; $rand(n)$ is a random number that satisfies the standard normal distribution; and k_j is the scaling factor, which usually takes values between 0.01 and 0.2.

(6) Elite retention strategies for superiority and inferiority. Parent and offspring individuals are selected to eliminate those that do not meet expectations, and the selected individuals become the parents of the next iteration.

The key hyperparameters of the evolutionary algorithm are set as: population size 24, maximum generations 35, stagnation generations 20, and 14 individuals per iteration. The crossover probability is 0.8, and the mutation probability is 0.01, as aforementioned.

Through the multi-objective evolutionary algorithm, the angle parameters β_1 and β_3 between the first rectangular PMs on the induced EMF fundamental waveform amplitude E_1, induced EMF waveform distortion rate THD_E, and cogging torque peak T_{cogmax} were obtained as shown in Figures 10(a), 10(b), and 10(c), respectively.

From Figures 10(a) and 10(b), when β_1 is taken as a fixed value, E_1 shows an obvious increasing trend with the increase of β_3, and the THD_E shows a tendency of decrease and then increase. When β_3 is considered a fixed value, E_1 and THD_E show a smaller tendency to change with changes in β_1. From Figure 10(c), in the range of $\beta_3 \in (50°, 80°)$, the maximum value of the cogging torque is lower.

The optimal solution set in multi-objective optimization is called the Pareto solution set, and the data points in the Pareto solution set represent the set of optimal solutions that can be obtained after trade-offs among multiple conflicting objectives [19]. The distribution of the optimization objective solution set obtained using the multi-objective evolutionary algorithm is shown in Figure 11.

All points in Figure 11 are simulation results calculated by the evolutionary algorithm, in which 55 data points form the

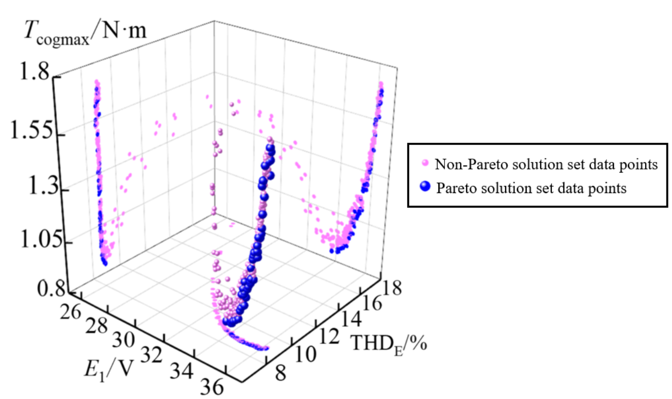

FIGURE 11. Distribution of the optimization objective solution set.

TABLE 3. TOPSIS evaluation of the Pareto solution set.

Number	E_1/V	THD_E/%	T_{cogmax}/N·m	Positive ideal distance	Negative ideal distance	Relative closeness	Sort
44	34.50	8.81	0.838	0.005	0.007	0.564	7
92	33.73	8.93	0.829	0.009	0.008	0.450	16
…	…	…	…	…	…	…	…
131	34.75	8.67	0.847	0.004	0.009	0.688	1
158	34.68	8.71	0.840	0.006	0.009	0.588	4
…	…	…	…	…	…	…	
325	34.89	8.75	0.869	0.008	0.008	0.483	13
332	35.01	8.71	0.871	0.008	0.009	0.516	10

Pareto solution set and stand for the optimal solutions after balancing the three optimization objectives. The screening points were further parsed and optimized using the technique for order preference by similarity to ideal solution (TOPSIS). The principle of the TOPSIS algorithm is as follows [20]:

(1) The screening points for n data objects and m evaluation indicators are presented in a matrix form with an initial matrix $X = [X_1, X_2, \ldots, X_j]$, where:

$$X_j = [x_{1j}, x_{2j}, \ldots, x_{nj}]^T, (j = 1, 2, \ldots, m) \tag{19}$$

(2) The reciprocal method is used to normalize negative indicators:

$$x'_{ij} = 1/x_{ij}(x_{ij} > 0), (i = 1, 2, \ldots, n) \tag{20}$$

(3) The data were processed using sum-of-squares normalization, and each evaluation indicator was made dimensionless, as shown in Equation (21):

$$\begin{cases} Z_j = [z_{1j}, z_{2j}, \ldots, z_{ij}]^T, & (j = 1, 2, \ldots, m) \\ z_{ij} = x'_{ij} \Big/ \sqrt{\sum\limits_{i=1}^{n} (x'_{ij})^2}, & (i = 1, 2, \ldots, n) \end{cases} \tag{21}$$

(4) Positive and negative ideals are computed for the post-processing matrix, and they can be expressed as:

$$\begin{cases} z^+ = [z_1^+, z_2^+, \ldots, z_m^+] \\ z^- = [z_1^-, z_2^-, \ldots, z_m^-] \\ z_j^+ = \max\{z_{1j}, z_{2j}, \ldots, z_{nj}\}, (j = 1, 2, \ldots, m) \\ z_j^- = \min\{z_{1j}, z_{2j}, \ldots, z_{nj}\}, (j = 1, 2, \ldots, m) \end{cases} \tag{22}$$

(5) Based on the ideal values, the positive and negative ideal distances of the screening points are calculated and expressed as:

$$\begin{cases} D_i^+ = \sqrt{\sum\limits_{j=1}^{m} \left(z_j^+ - z_{ij}\right)^2} \\ D_i^- = \sqrt{\sum\limits_{j=1}^{m} \left(z_j^- - z_{ij}\right)^2} \end{cases} \tag{23}$$

(6) Based on the positive and negative ideal distances of each screening point, the relative proximity c_i was calculated. The larger the c_i is, the better the optimization result of the point is. c_i can be expressed as:

$$c_i = \frac{D_i^-}{D_i^+ + D_i^-}, (0 < c_i < 1) \tag{24}$$

The TOPSIS evaluation of the Pareto solution set data points is presented in Table 3.

From Table 3, the data point numbered 131 is the closest to the relative ideal value, and its corresponding optimization parameters are $\beta_1 = 49°$ and $\beta_3 = 76°$. Based on the optimal solutions for β_1 and β_3, a single-parameter scanning method was used to determine the optimal value of β_2. The influence patterns of parameter β_2 on E_1, THD_E, and T_{cogmax} are shown in Figures 12(a), 12(b), and 12(c), respectively.

As shown in Figure 12, as β_2 increases, E_1, THD_E, and T_{cogmax} show an increasing trend, and when $\beta_2 > 72°$, the tendency of T_{cogmax} to increase with the increase of β_2 is gradually intensified, with the optimal β_2 taken as 72°.

4.3. Single Parameter Scanning Optimization of PM Size Based on Performance-to-Cost Ratio Indices

The width and thickness of PMs directly affect the MMF and magnetic flux of PMGs, which in turn affect the generator-induced EMF; however, the volume of PMs is not the larger, the better. The size of the induced EMF and the number of PMs do not show a linear relationship, and an excessive number of PMs not only increases generator manufacturing cost but also results in the waste of PMs [21]. Therefore, to improve output performance and reduce manufacturing cost of rare-earth-saving PMGs, the width and thickness parameters of each PM must be further optimized and analyzed.

In this study, a performance-to-cost ratio index is proposed to measure the magnitude of the fundamental amplitude of the induced EMF versus PM cost. The performance-to-cost ratio index K_{pm} is defined as follows:

$$K_{pm} = \frac{E_1}{M} \tag{25}$$

The larger the performance-to-cost ratio index K_{pm} is, the larger the fundamental amplitude of the induced EMF per unit cost, and the better the generator performance. Based on the

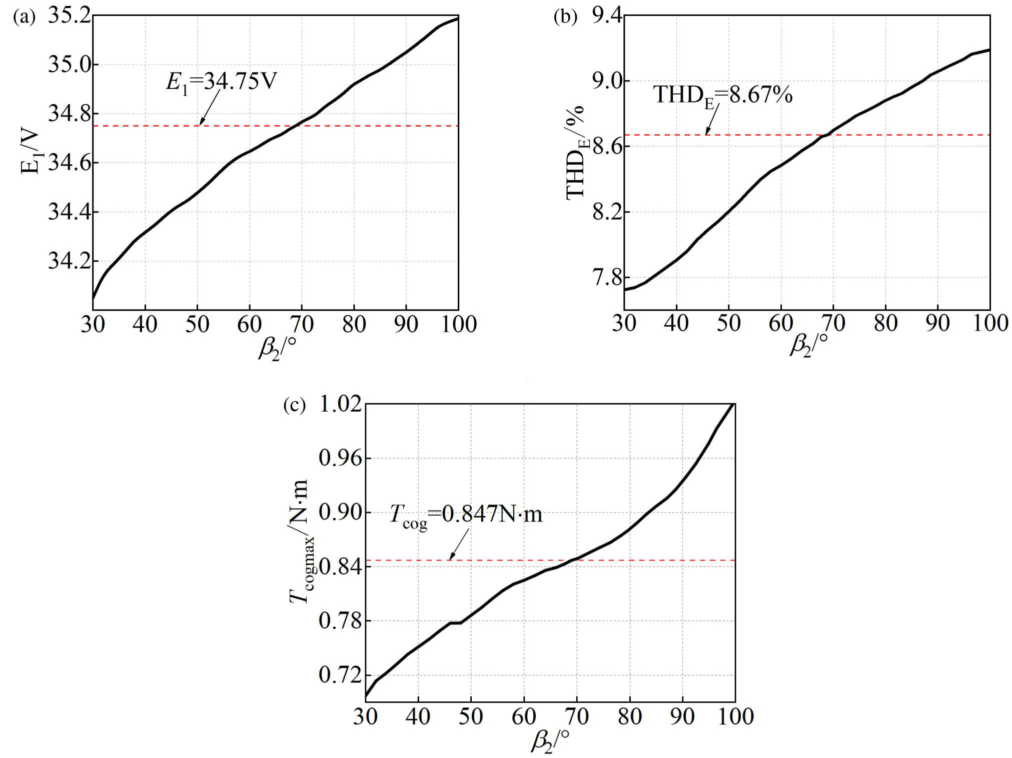

FIGURE 12. Influence patterns of the parameter β_2 on E_1, THD_E and T_{cogmax}. (a) E_1, (b) THD_E, and (c) T_{cogmax}.

optimal PM pinch angle parameters determined in the optimization process above, the optimization range of each rectangular PM width and thickness parameter was determined, as shown in Table 4.

TABLE 4. Optimization range of each rectangular PM width and thickness.

Parameter	Definition	Range
b_1/mm	Width of the first rectangular PM	[12, 17]
b_2/mm	Width of the second rectangular PM	[4, 6]
b_3/mm	Width of the third rectangular PM	[9, 13]
w_1/mm	Thickness of the first rectangular PM	[2.5, 4]
w_2/mm	Thickness of the second rectangular PM	[1.2, 2]
w_3/mm	Thickness of the third rectangular PM	[1.5, 3.5]

Analyze the influence of each rectangular PM width and thickness parameter on the optimization objectives. The influence of each rectangular PM width parameter on the optimization objective is illustrated in Figure 13.

From Figure 13(a), both E_1 and THD_E of the rare-earth-saving PMG increase as b_1 increases. When $b_1 \geq 16.0$ mm, the tendency of THD_E increases as b_1 increases. When $b_1 \geq 14.0$ mm, E_1 was at a higher level. To select the optimal value of b_1, the parameter K_{pm} for data points in the range of $14.0\,\text{mm} \leq b_1 \leq 16.0\,\text{mm}$ were compared. The b_1 corresponding to the maximum value of K_{pm} was selected as the optimal solution. The results show that $K_{pm} = 0.4769$, at $b_1 = 15.5$ mm, is the maximum value of K_{pm} in the optimized range; therefore, b_1 is taken as 15.5 mm.

From Figure 13(b), E_1 of the rare-earth-saving PMG increases with an increase in b_2. THD_E decreases and then increases with an increase in b_2, and the turning point of the trend of the change in THD_E is $b_2 = 5.5$ mm. To select the optimal value of b_2, the parameter K_{pm} for data points in the range of $5.5\,\text{mm} \leq b_2 \leq 6.0\,\text{mm}$ are compared. The results show that at $b_2 = 5.5$ mm, $K_{pm} = 0.4792$ is the maximum value in the optimized range; therefore, b_2 is taken as 5.5 mm.

As shown in Figure 13(c), E_1 of the rare-earth-saving PMG increases as b_3 increases; THD_E decreases and then increases; and the turning point of the changing trend of THD_E is $b_3 = 12.0$ mm. To select the optimal value of b_3, the parameter K_{pm} for data points in the range of $12.0\,\text{mm} \leq b_3 \leq 13.0\,\text{mm}$ were compared. The results show that $K_{pm} = 0.4826$, at $b_3 = 13.0$ mm, is the maximum value in the optimized range; therefore, b_3 is taken as 13.0 mm.

The influence of each rectangular PM thickness parameter on the optimization objective is illustrated in Figure 14.

As shown in Figure 14(a), E_1 of the rare-earth-saving PMG increases with an increase in w_1. THD_E decreases and then increases with the increase of w_1, and the turning point of the trend of the change of THD_E is $w_1 = 3.2$ mm. To select the optimal value of w_1, the parameter K_{pm} for data points in the range of $3.2\,\text{mm} \leq w_1 \leq 4.0\,\text{mm}$ are compared. The results show that at $w_1 = 3.2$ mm, $K_{pm} = 0.4828$ is the maximum value in the optimized range; therefore, w_1 is taken as 3.2 mm.

From Figure 14(b), E_1 of the rare-earth-saving PMG increases with an increase in w_2. THD_E decreases and then increases with an increase in w_2, and the turning point of the trend of the change in THD_E is $w_2 = 1.6$ mm. To select the

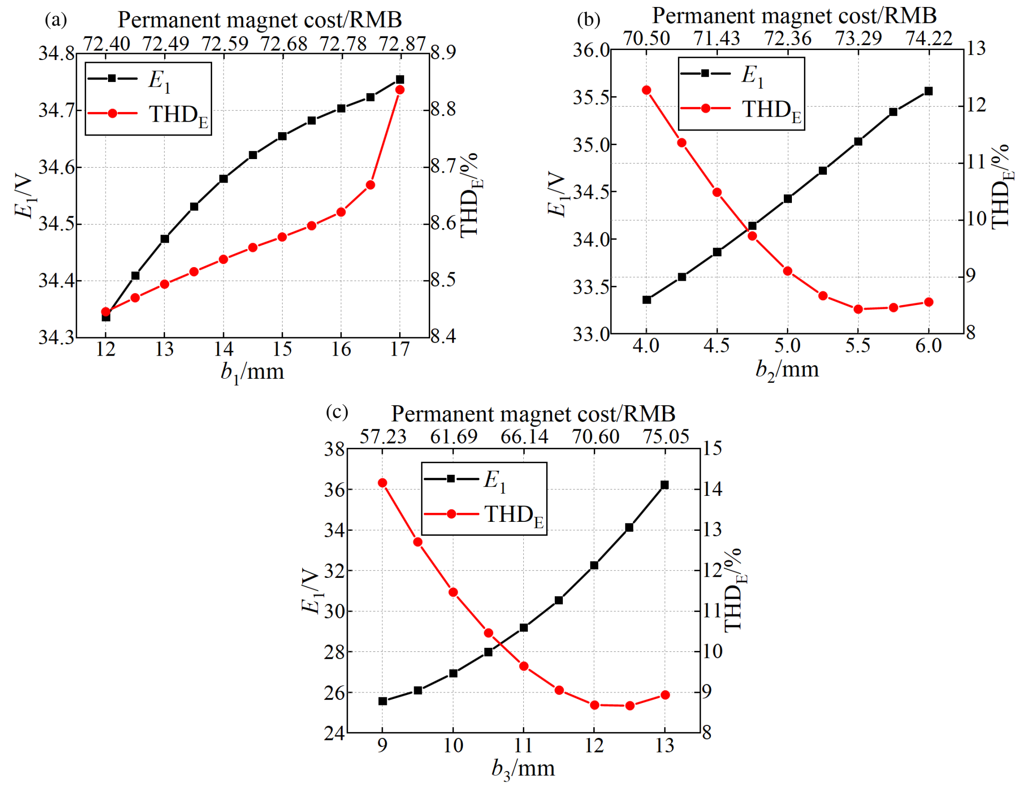

FIGURE 13. Influence of each rectangular PM width parameter on the optimization objective. (a) b_1, (b) b_2, and (c) b_3.

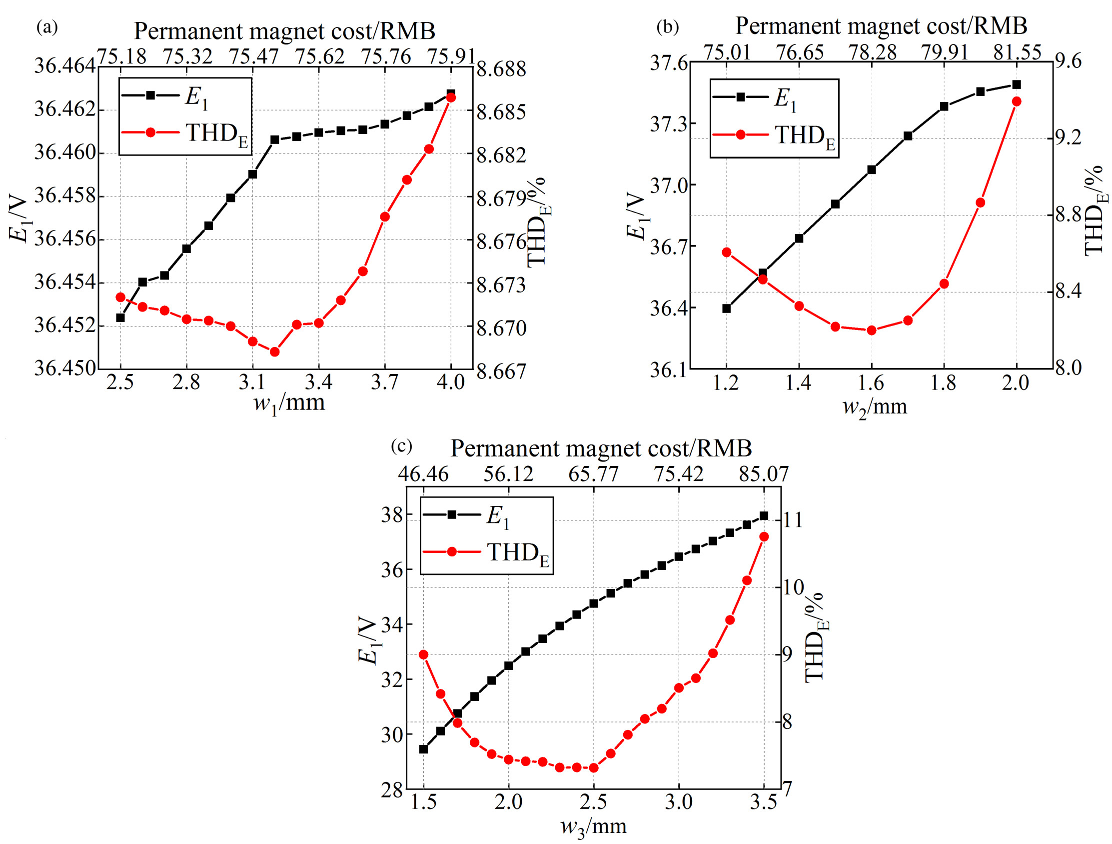

FIGURE 14. Influence of each rectangular PM thickness parameter on the optimization objective. (a) w_1, (b) w_2, and (c) w_3.

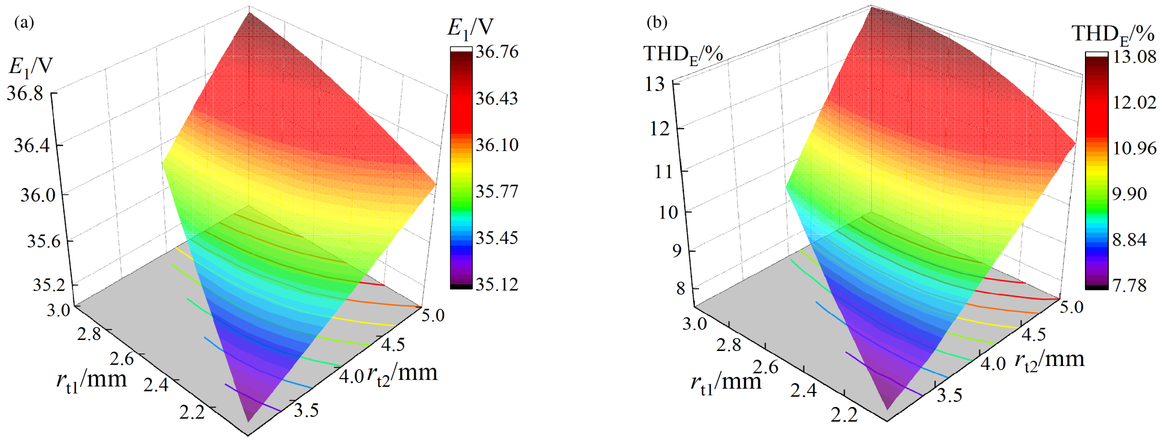

FIGURE 15. Influence law of the radius parameter of the arc-shaped PM on the optimization objective. (a) E_1 and (b) THD_E.

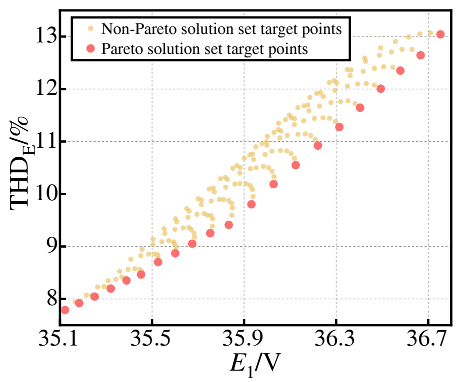

FIGURE 16. Distribution of solution set for the optimization objective.

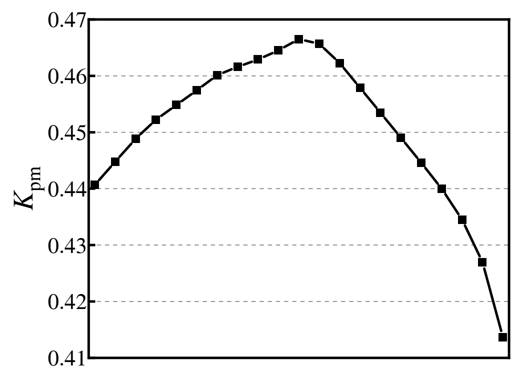

FIGURE 17. K_{pm} in Pareto solution set.

optimal value of w_2, the parameter K_{pm} for data points in the range of $1.6\,\text{mm} \leq w_2 \leq 2.0\,\text{mm}$ were compared. The results show that at $w_2 = 1.6\,\text{mm}$, $K_{pm} = 0.4736$ is the maximum value in the optimized range; therefore, w_2 is taken as 1.6 mm.

From Figure 14(c), E_1 of the rare-earth-saving PMG increases as w_3 increases; THD_E shows a trend of decrease and then increase; and the turning point of the changing trend of THD_E is $w_3 = 2.5\,\text{mm}$. To select the optimal value of w_3, the parameter K_{pm} for data points in the range of $2.5\,\text{mm} \leq w_3 \leq 3.5\,\text{mm}$ were compared. The results show that at $w_3 = 2.5\,\text{mm}$, $K_{pm} = 0.5284$ is the maximum value in the optimized range; therefore, w_3 is taken as 2.5 mm.

Based on the optimal parameter combination of the rectangular PM, the inner and outer radii of the arc-shaped PM were further optimized. Owing to the structure's special characteristics, the inner and outer radii of the arc-shaped PM affect both the width and thickness of the PM, which should be optimized simultaneously. To ensure the reliability of PM manufacturing, the difference between the inner and outer radii of the arc-shaped PM should be greater than or equal to 1 mm, that is, $r_{t2} - r_{t1} \geq 1\,\text{mm}$. The influence of the radius parameter of the arc-shaped PM on the optimization objective is shown in Figure 15.

From Figure 15, the influence laws of rare-earth-saving PMGs r_{t1} and r_{t2} on E_1 and THD_E are approximately the same, and as r_{t1} and r_{t2} increase, E_1 and THD_E also increase. The optimal parameters of the arc-shaped PM cannot be determined only by the laws of r_{t1} and r_{t2} on E_1 and THD_E. The distribution solution set of the optimization objective E_1 and THD_E corresponding to each data point was analyzed, and the preferred solution set of the Pareto front in the solution set of the optimization objective was screened out, as shown in Figure 16.

The optimization objective solution set consists of target points from both the non-Pareto solution set and the Pareto solution set, and there are 21 data points in the Pareto solution set corresponding to all data points, as shown in Figure 16. The K_{pm} values are compared for the 21 data points in the Pareto solution set, as shown in Figure 17.

From Figure 17, there is a peak in the variation curve of the K_{pm} at the data points in the Pareto solution set, and the peak data point corresponds to the radius parameters of the arc-shaped PM as $r_{t1} = 2.0\,\text{mm}$, $r_{t2} = 3.4\,\text{mm}$, and $K_{pm} = 0.4665$ at that point. Therefore, r_{t1} and r_{t2} were taken as 2.0 mm and 3.4 mm, respectively.

4.4. Comparison of Generator Performance Before and After Multi-Objective Optimization

To verify the reliability of the optimization scheme of rare-earth-saving PMGs and the correctness of the theoretical anal-

TABLE 5. Parameters of rare-earth-saving PMGs before and after optimization.

Parameter	Before optimization	After optimization	Parameter	Before optimization	After optimization
$\beta_1/°$	72	49	w_2/mm	1.3	1.6
$\beta_2/°$	100	72	w_3/mm	3.0	2.5
$\beta_3/°$	72	76	b_1/mm	12.6	15.5
r_{t1}/mm	2.7	2.0	b_2/mm	5.4	5.5
r_{t2}/mm	4.0	3.4	b_3/mm	12.6	13.0
w_1/mm	3.0	3.2			

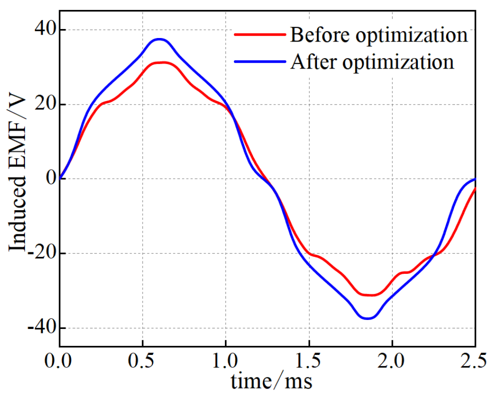

FIGURE 18. Induced EMF before and after optimization.

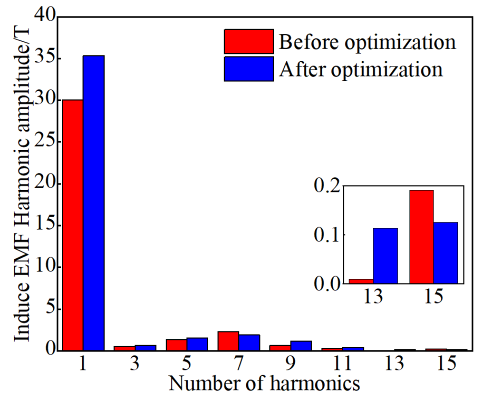

FIGURE 19. Induce EMF Harmonic amplitude before and after optimization.

ysis, a comparative analysis of the performance of rare-earth-saving PMGs before and after optimization was conducted, as shown in Table 5.

A comparative analysis of the induced EMF and cogging torque before and after the optimization of the rare-earth-saving PMG is shown in Figures 18 and 19.

As shown in Figures 18 and 19, compared with pre-optimization, the fundamental amplitude of the induced EMF after optimization increased from 30.06 to 35.34 V, which is 17.56%. The waveform amplitude of the induced EMF increased from 31.36 to 37.53 V, which is 19.67%. The THD of the induced EMF before and after optimization was calculated to be 8.95% and 8.44%, respectively. The THD of the EMF waveform after optimization was reduced by 5.70%. The change in the induced EMF before and after optimization is approximately the same as that of the air-gap flux density. The enhancement of the fundamental amplitude and reduction of the THD of the rare-earth-saving PMG-induced EMF are achieved by multi-objective hierarchical optimization.

Before optimization, the total amount of ferrite was 34020 mm^3, and the total amount of NdFeB was 46494.74 mm^3; after optimization, the total amount of ferrite was 44640 mm^3, and the total amount of NdFeB was 42513.85 mm^3. The optimized rare-earth-saving PMG not only has a higher fundamental amplitude of induced EMF and lower THD, but also has lower NdFeB consumption. Through multi-objective hierarchical optimization, the number of NdFeB PMs was reduced while improving generator output performance.

The waveforms of the cogging torque before and after optimization of the rare-earth-saving PMG are shown in Figure 20.

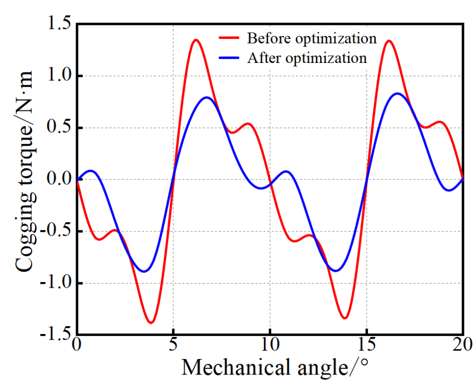

FIGURE 20. Cogging torque before and after optimization.

As shown in Figure 20, compared with the pre-optimization, the maximum value of the cogging torque after optimization was reduced from 1.42 N·m to 0.83 N·m, representing a 41.55% decrease. Additionally, the cogging torque waveform values after optimization were lower than those before optimization. The cogging torque of the rare-earth-saving PMG was reduced by optimizing asymmetric poles.

5. PROTOTYPING AND TESTING

According to the optimal structural parameters of the rare-earth-saving PMG, a prototype with a rated power of 1000 W,

FIGURE 21. Generator prototype. (a) Rotor core, (b) rotor, (c) stator core, (d) stator, and (e) prototype.

rated output voltage of 28 V, and rated speed of 4000 rpm was fabricated, as shown in Figure 21.

5.1. Rare-Earth-Saving PMG Output Performance Test

To verify the output performance of the rare-earth-saving PMG, a test bench was built to conduct a prototype output performance test, as shown in Figure 22.

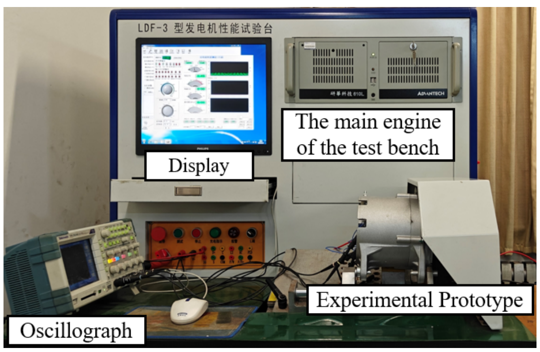

FIGURE 22. Output performance test bench.

Under no-load conditions, the prototype speed was set to 4000 r/min, and the no-load three-phase EMF at the rated speed was tested, as shown in Figure 23.

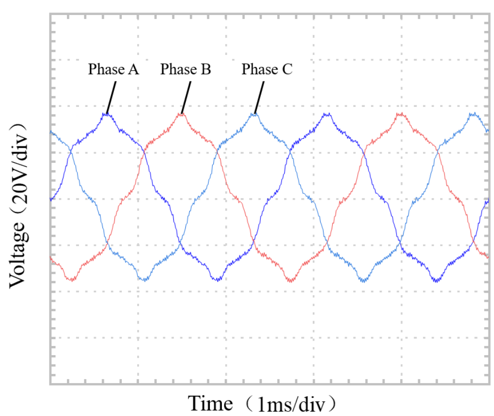

FIGURE 23. No-load three-phase EMF at a rated speed.

From Figure 23, under rated speed condition, the three-phase EMF waveforms are symmetrical in shape, with a phase angle difference of 120°. The test waveforms were similar to the simulation, and the amplitude of the phase voltage waveforms was 37.12 V, which differed from the simulation result of 37.53 V by 0.41 V, with a relative error of approximately 1.09%.

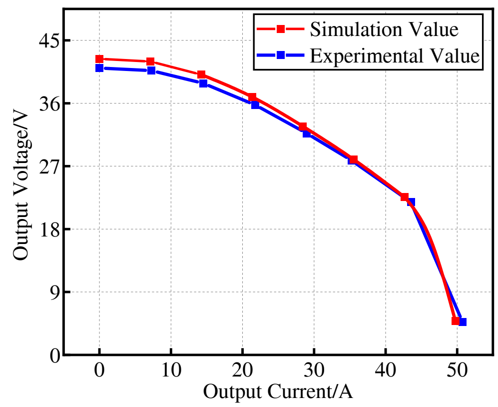

FIGURE 24. Comparison of external characteristic curves.

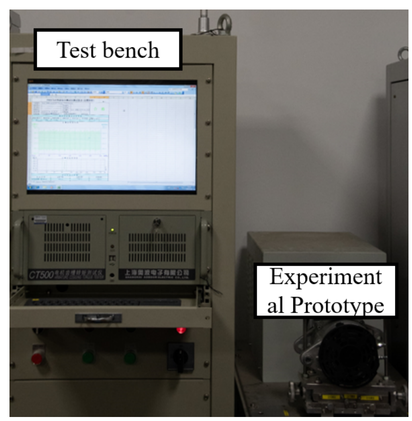

FIGURE 25. Cogging torque test bench.

An electronic resistive load is mounted on the DC output terminal of the generator test bench for load characteristic tests. The generator operates at rated speed, and the load resistance is varied to record the output voltage and current under various load powers. The external characteristic curves of the low-rare-earth PMG are drawn and compared with simulated results, as illustrated in Figure 24.

As shown in Figure 24, the external characteristic curves of the low-rare-earth PMG from prototype tests and simulations share nearly identical variation rules. Larger output current in prototype tests under the same load brings stronger armature reaction, lowering the generator output voltage. The maximum relative errors of the output voltage and output current between the test and simulation are 3.10% and 2.01%, respectively. The minor deviations confirm the validity of the simulation.

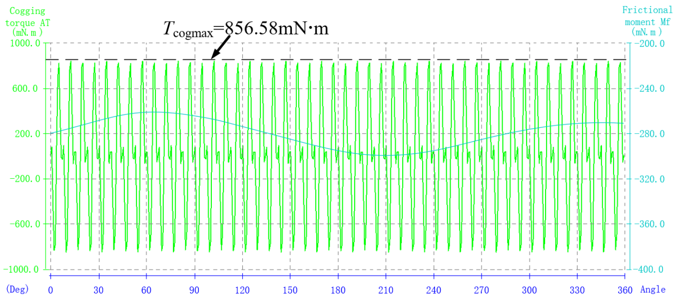

FIGURE 26. Rare-earth-saving PMG cogging torque test waveform.

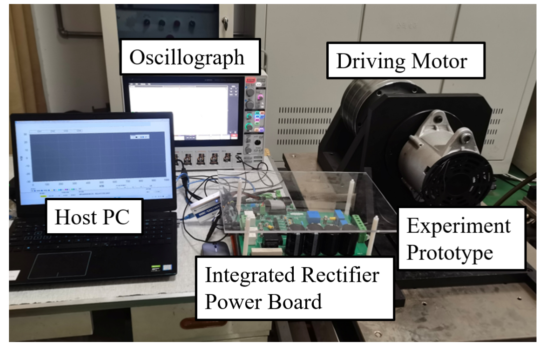

FIGURE 27. Voltage stabilization control test platform.

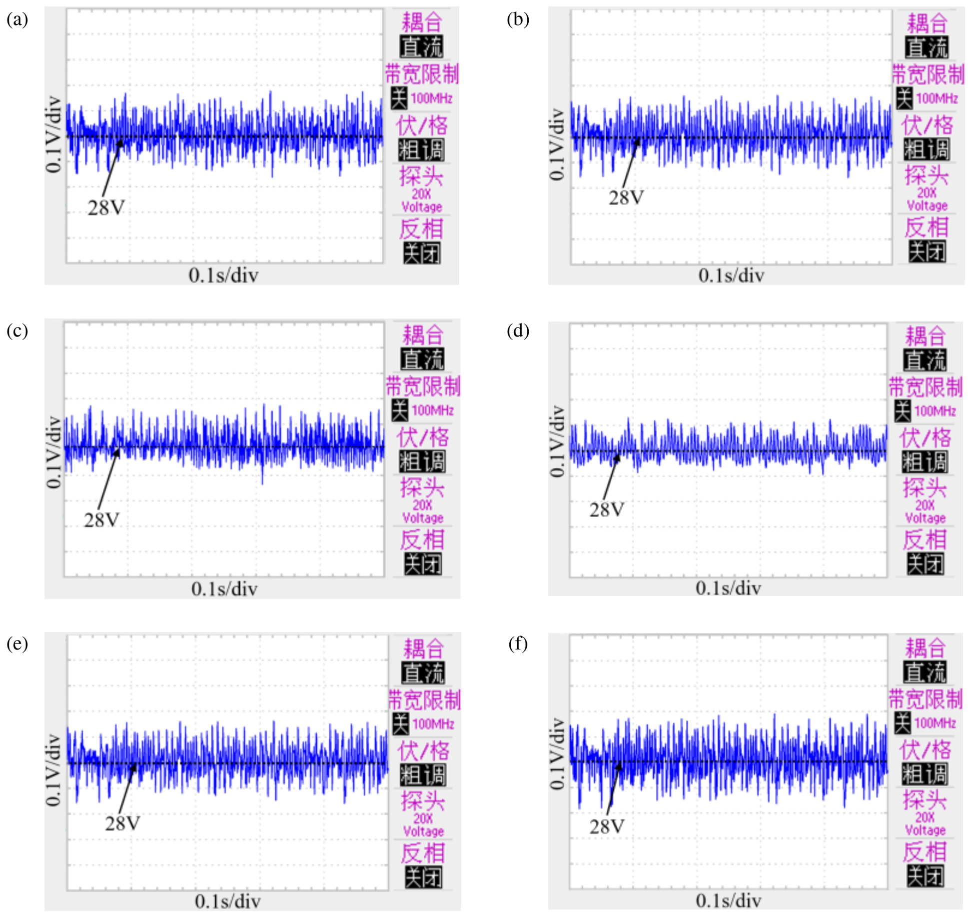

FIGURE 28. The output voltage waveforms under different rotational speeds and load conditions. (a) 2400 r/min 1000 W, (b) 4000 r/min 1000 W, (c) 4800 r/min 1000 W, (d) 4000 r/min 500 W, (e) 4000 r/min 1000 W, and (f) 4000 r/min 1200 W.

5.2. Rare-Earth-Saving PMG Cogging Torque Test

The cogging torque of the rare-earth-saving PMG was tested using a cogging torque test bench, as shown in Figure 25. The prototype was fastened to the test bench, and the motor shaft and sensor were mounted coaxially and side by side using a coupling. The prototype was slowly rotated by the servo motor in the tester, which could extract the signal of the generator's cogging torque. The rare-earth-saving PMG cogging torque test waveform is illustrated in Figure 26.

From Figure 25, the maximum cogging torque is 856.58 mN·m, which is 41.85 mN·m different from the simulation results of 834.73 mN·m. The relative error was approximately 2.62%, which is relatively small. The cogging torque test results validate the correctness of the theoretical analysis of the magnetic poles and the effectiveness of the structural optimization.

5.3. Rare-Earth-Saving PMG Voltage Stabilization Control Test

The voltage regulation performance of the generator under the AC-DC voltage stabilization scheme based on a three-phase voltage-source PWM rectifier is tested. A voltage stabilization control test bench is established to measure the DC-side output voltage of the low-rare-earth PMG. The voltage stabilization control test platform is shown in Figure 27, and the output voltage waveforms under different rotational speeds and load conditions are illustrated in Figure 28.

It can be seen from Figures 28(a)–28(c) that the DC voltage ripple decreases with the increase of rotational speed. The DC-side output voltage can be stabilized within $28\,\mathrm{V} \pm 0.2\,\mathrm{V}$ under all tested speed conditions. When the generator operates at 2400 r/min, the ripple factor of the DC voltage is 1.27%.

As shown in Figures 28(d)–28(f), the DC voltage ripple rises as the load increases. The DC-side output voltage remains within $28\,\mathrm{V} \pm 0.2\,\mathrm{V}$ for all load conditions. Under the overload condition of 1250 W on the DC side, the DC voltage ripple factor reaches 1.34%.

The experimental results demonstrate that the low-rare-earth PMG can deliver stable DC output voltage under complex operating conditions with a wide range of rotational speeds and loads.

6. CONCLUSIONS

To address the issues of high rare-earth PMs and high cogging torque in traditional symmetric-pole PMGs, a rare-earth-saving combined-pole structure for automotive PMGs using NdFeB and ferrite for co-excitation is proposed. Based on the energy method and an established equivalent magnetic circuit model, the mechanism by which the asymmetrical pole structure improves the air-gap magnetic flux density and reduces the cogging torque is derived. Considering the angle, width, and thickness of PMs as optimization parameters, an evolutionary algorithm combined with the TOPSIS method is used to optimize the angle of PMs, and the width and thickness of PMs are optimized according to the performance cost ratio index to realize the multi-objective optimization of rare-earth-saving PMGs with asymmetric magnetic poles. Finally, a prototype was tested and verified according to the optimized dimensions, and the following conclusions were drawn:

1) The MMF of PMs directly affects the air-gap magnetic flux density and cogging torque of the generator, which in turn affects the generator-induced EMF. The construction of asymmetric poles can reduce the cogging torque by increasing the fundamental amplitude and reducing the generator's THD. The rare-earth-saving PMG has optimal performance when $\beta_1 = 49°$, $\beta_2 = 72°$, and $\beta_3 = 76°$.

2) The optimal performance output of rare-earth-saving PMG can be achieved by optimizing the size and arrangement of the four groups of PMs using multi-objective optimization. Compared with pre-optimization, the post-optimization induced EMF fundamental waveform amplitude improved by 17.56%, the induced EMF waveform amplitude improved by 19.67%, the induced EMF waveform THD reduced by 5.70%, the cogging torque reduced by 41.55%, and the total NdFeB usage reduced by 8.56%. The combined excitation of NdFeB and ferrite PMs reduced the number of NdFeB PMs used while improving generator performance.

ACKNOWLEDGEMENT

This work was supported in part by the National Natural Science Foundation of China under Grant 52275261 and Grant 52505269 and in part by the Natural Science Foundation of Shandong Province of China under Grant ZR2025MS914.

REFERENCES

[1] Darwish, A., M. A. Elgenedy, and B. W. Williams, "A review of modular electrical sub-systems of electric vehicles," *Energies*, Vol. 17, No. 14, 3474, 2024.

[2] Prakht, V., V. Dmitrievskii, and V. Kazakbaev, "Analysis of performance improvement of passenger car synchronous homopolar generator with the addition of ferrite magnets," *Applied Sciences*, Vol. 13, No. 6, 3990, 2023.

[3] Liu, J., X. Zhu, L. Quan, Z. Xiang, and C. Zhang, "Driving control research of less-rare-earth tooth yoke magnetomotive complementary doubly salient permanent magnet motors based on resonance compensation strategy," *Proceedings of the CSEE*, Vol. 37, No. 22, 6534–6542, 2017.

[4] Si, X., X. Zhu, Y. Zuo, Z. Xiang, and L. Xu, "Research on drive performance of the less-rare-earth hybrid-excitation PM motor based on decoupled SVPWM control strategy," *Proceedings of the CSEE*, Vol. 40, No. 24, 7899–7909, 2020.

[5] Li, F., K. Wang, X. Song, J. Li, S. Zhu, and C. Liu, "Coordinated control with high efficiency in wide operating region of AC-excited hybrid excitation generator," *Proceedings of the CSEE*, Vol. 45, No. 10, 4046–4055, 2025.

[6] Ma, X., Q. Zheng, X. Han, and T. Zhou, "Optimal design of the pole structure of low head permanent magnet synchronous generators," *Electrical Machinery Technology*, No. 3, 5–10, 2024.

[7] Zhen, Z., H. Wang, X. Han, Y. Fan, and Q. U. Guangyu, "Design and analysis of a consequent-pole permanent magnet wind generator," *Micromotors*, Vol. 52, No. 8, 2019.

[8] Wang, X., H. Yin, and R. Yu, "Magnetic field analysis and rotor optimization for coreless axial flux permanent magnet synchronous machine," *Electric Machines and Control*, Vol. 28, No. 9, 170–178, 2024.

[9] Afinowi, I. A. A., Z. Q. Zhu, Y. Guan, J.-C. Mipo, and P. Farah, "Switched-flux machines with hybrid NdFeB and ferrite magnets," *COMPEL: The International Journal for Computation and Mathematics in Electrical and Electronic Engineering*, Vol. 35, No. 2, 456–472, 2016.

[10] Khazdozian, H. A., R. L. Hadimani, and D. C. Jiles, "Development of rare earth free permanent magnet generator using halbach cylinder rotor design," *Renewable Energy*, Vol. 112, 84–92, 2017.

[11] Shao, P., J. Xu, Q. Liang, and Y. Zhang, "Analytical modeling of magnetic field of permanent magnet in surface mounted linear motors based on exact subdomain model method," *Journal of Naval University of Engineering*, Vol. 36, No. 3, 66–71, 2024.

[12] Xing, Z. Z., X. H. Wang, and W. L. Zhao, "Research on reduction methods of cogging torque based on segmented skewing magnetic poles with different combinations of pole-arc coefficients in surface-mounted permanent magnet synchronous motors," *Proceedings of the CSEE*, Vol. 41, No. 16, 5737–5748, 2021.

[13] Wang, W., X. Zhang, C. Yu, J. Zhang, S. Hua, K. Geng, and W. Hu, "Research on cogging torque weakening method of parallel double-rotor motor based on polar arc coefficient and relative deflection angle of rotor," *Journal of Shaanxi University of Science & Technology*, Vol. 41, No. 6, 139–144,154, 2023.

[14] Bao, M., Y. Sun, C. Chen, and X. Zheng, "Calculation of suspension force of amorphous alloy high-speed maglev linear motor based on distributed magnetic circuit method," *Transactions of China Electrotechnical Society*, Vol. 38, No. 14, 3678–3688,3732, 2023.

[15] Song, S.-W., M.-K. Hong, J. Lee, and W.-H. Kim, "A study on reduction of cogging torque and magnet usage through intersect magnet consequent pole structure," *Energies*, Vol. 15, No. 23, 9255, 2022.

[16] Geng, H., X. Zhang, T. Si, L. Tong, Q. Ma, and M. Xu, "Analysis of the rotor magnetomotive force of built-in radial permanent magnet generator for vehicle," *International Journal of Rotating Machinery*, Vol. 2021, No. 1, 5319615, 2021.

[17] Liang, Z. and X. Liu, "Equivalent dynamic magnetic network model of novel disc planetary permanent magnet motor," *Journal of Zhejiang University(Engineering Science)*, Vol. 58, No. 10, 2182–2191, 2024.

[18] Mamede, A. C. F. and J. R. Camacho, "Evolutionary algorithms for optimization of 4/4 single phase switched reluctance machine," *IEEE Latin America Transactions*, Vol. 16, No. 6, 1684–1691, 2018.

[19] Yang, L., J. Xu, J. Chen, J. Li, and S. Xiang, "An analysis model of renewal regulation policy for village-in-city based on pareto optimality theory: A case study of zhuhai city," *Urban Development Studies*, Vol. 30, No. 8, 68–75, 2023.

[20] Zhou, D., L. Lu, C. Yang, Y. Dai, and X. Wang, "Co-simulation optimization of high speed permanent magnet synchronous motor based on genetic algorithm and TOPSIS method," *Modular Machine Tool & Automatic Manufacturing Technique*, Vol. 11, 69–73, 2023.

[21] Jiang, L., L. Yang, L. Chen, and F. Xie, "Research on less-rare-earth hybrid permanent magnet synchronous motor for industrial robots," *Small & Special Electrical Machines*, Vol. 53, No. 5, 21–26.